CrossMark

J. Fluid Mech. (2017), *vol.* 826, *pp.* 797–818. © Cambridge University Press 2017
doi:10.1017/jfm.2017.443

Axisymmetric viscous interfacial oscillations – theory and simulations

Palas Kumar Farsoiya[1], Y. S. Mayya[1] and Ratul Dasgupta[1,†]

[1]Department of Chemical Engineering, Indian Institute of Technology, Bombay Powai, Mumbai 400 076, India

(Received 27 March 2017; revised 19 May 2017; accepted 19 June 2017; first published online 15 August 2017)

We study axisymmetric, free oscillations driven by gravity and surface tension at the interface of two viscous, immiscible, radially unbounded fluids, analytically and numerically. The interface is perturbed as a zeroth-order Bessel function (in space) and its evolution is obtained as a function of time. In the linearised approximation, we solve the initial value problem (IVP) to obtain an analytic expression for the time evolution of wave amplitude. It is shown that a linearised Bessel mode temporally evolves in exactly the same manner as a Fourier mode in planar geometry. We obtain novel analytical expressions for the time varying vorticity and pressure fields in both fluids. For small initial amplitudes, our analytical results show excellent agreement with those obtained from solving the axisymmetric Navier–Stokes equations numerically. We also compare our results with the normal mode approximation and find the latter to be an accurate representation at very early and late times. The deviation between the normal mode approximation and the IVP solution is found to increase as a function of viscosity ratio. The vorticity field has a jump discontinuity at the interface and we find that this jump depends on the viscosity and the density ratio of the two fluids. Upon increasing the initial perturbation amplitude in the simulations, nonlinearity produces qualitatively new features not present in the analytical IVP solution. Notably, a jet is found to emerge at the axis of symmetry rising to a height greater than the initial perturbation amplitude. Increasing the perturbation amplitude further causes the jet to undergo end pinch off, giving birth to a daughter droplet. This can happen either for an advancing or a receding jet, depending on the viscosity ratio. A relation is found between the maximum jet height and the perturbation amplitude. Hankel transform of the interface demonstrates that at large perturbation amplitudes higher wavenumbers emerge, sharing some of the energy of the lowest mode. When these additional higher modes are present, the interface has pointed crests and rounded troughs.

Key words: capillary waves, multiphase flow, surface gravity waves

1. Introduction

Waves at the interface of two immiscible viscous fluids have been of interest to the fluid dynamics community for technological applications such as drug delivery (Tsai *et al.* 2014) as well as from a fundamental perspective in understanding nonlinear

† Email address for correspondence: dasgupta.ratul@iitb.ac.in

https://doi.org/10.1017/jfm.2017.443 Published online by Cambridge University Press

systems and phenomena such as atomisation (Puthenveettil & Hopfinger 2009; Li & Umemura 2014). Dating from the seminal study by Michael Faraday (Faraday 1831), forced standing interfacial oscillations have received continued interest and attention in the fluid dynamics literature having become a canonical system for studying nonlinear physics and pattern formation in parametrically forced systems (Perinet, Juric & Tuckerman 2009; Rajchenbach & Clamond 2015). A study of such oscillations, especially the ones occurring in cylindrical geometries, has significant practical utility. They appear during sloshing in partially liquid-filled cylindrical containers subject to vertical vibration (Henderson & Miles 1994). Atomisation as a result of instabilities of standing waves appearing on a vibrated sessile droplet have been proposed as a technique for spray cooling of microprocessors (James *et al.* 2003). Axisymmetric free interfacial oscillations similarly have many applications. At large scales, where surface tension and viscous effects are negligible, they are relevant for understanding seiches in harbours (Mack 1962). The well-known Cauchy–Poisson problem in water waves (Debnath 1994) can be analysed as a linear superposition of axisymmetric standing modes excited by initial conditions (Miles 1968). At smaller laboratory scales involving smaller wavelengths and highly viscous fluids, gravity, surface tension and viscosity can significantly influence the time evolution, deformation and subsequent break-up of these interfacial waves (Goodridge *et al.* 1997). Early comparisons of experiments on standing waves with nonlinear, inviscid, irrotational theory were made by Taylor (1953) and Thorpe (1968). A comparison of theoretical damping calculations of free oscillations with experiments was reported by Miles & Henderson (1990) in a confined cylindrical geometry. For a highly viscous fluid *viz.* paraffin oil, Bechhoefer *et al.* (1995) conducted experiments on Faraday waves in cylinders finding that for sufficient size, oscillations behave as if they are occurring in radially unbounded geometry.

The dispersion relation for irrotational, small-amplitude interfacial waves on unbounded fluids in a planar geometry has been long known (Lamb 1932) and is readily obtainable from normal mode analysis. The addition of viscosity into the normal mode approximation was done by Harrison (1908) (also see Lamb (1932), Chandrasekhar (1961)). The viscous normal mode eigenfunctions however do not form a complete set (Lamb 1932) and the spectrum has an additional continuous part, for which no dispersion relation exists (Lamb 1932; Balmforth & Morrison 1995). Thus one cannot solve the initial value problem (IVP) for general initial conditions by expanding these in the normal mode eigenfunctions alone. This lacuna was rectified in Prosperetti (1976), Menikoff *et al.* (1978), Prosperetti (1981) who solved the planar IVP for a single spatial Fourier mode using Laplace transform in time. It was demonstrated that in addition to normal mode terms arising from the discrete part of the spectrum, the viscous spectrum has a continuous part which leads to terms with non-exponential dependence on time. In a planar geometry and for capillary waves, a comparison of the IVP solution of Prosperetti (1981) with direct numerical simulation (DNS) of the Navier–Stokes equation for small perturbation amplitude has been reported in Popinet (2013), Denner (2016) and a good match has been observed. Using scaling arguments, Denner (2016) also showed that for small-amplitude under-damped capillary oscillations, independent of the viscosity and density ratio of the two fluids, a single non-dimensional frequency can be obtained for a given non-dimensional wavenumber. The critical wavenumber used for this collapse was obtained using a damped simple harmonic oscillator model for the interface. Further extension of this work to include finite-amplitude capillary waves has been recently reported in Denner, Paré & Zaleski (2017*a*) where an empirical correlation is

https://doi.org/10.1017/jfm.2017.443 Published online by Cambridge University Press

obtained for the effect of wave amplitude on viscous dissipation. Using this correlation to correct for finite-amplitude effects, it has been shown (Denner *et al.* 2017*a*) that the capillary wave dispersion relation is self-similar for finite-amplitude waves as well. In cylindrical axisymmetric radially bounded geometries, inviscid, irrotational interfacial oscillations have been analysed in Drazin & Reid (2004) (see problem 1.12) using normal modes. In the presence of a confining cylindrical boundary, a viscous normal mode study has been reported in Sweeney, Kerswell & Mullin (2013). The only study of the IVP for radially unbounded cylindrical geometry is by Miles (1968) who obtained analytical results for certain initial conditions. His solution however neglects the inertia and viscosity of the upper fluid, whose effect in certain parametric regimes can be large. The solution to the axisymmetric IVP involving inertia and viscosity of both fluids has not been reported in the literature before and is done here. It is shown that a small-amplitude axisymmetric Bessel mode temporally evolves in exactly the same way as a planar Fourier mode. Detailed comparisons of DNS results, the normal mode solution and the IVP for a range of non-dimensional parameters are reported here for the first time. The paper is organised as follows: In § 2 we solve the IVP. Results from the normal mode approximation are provided in § 3 followed by a description of simulations in § 4. Results, comparisons and analysis are presented in § 5. We conclude with a discussion and future scope of work.

2. Viscous initial value problem

In this section, we derive the equation governing the time evolution of the interface initiated as an axisymmetric zeroth-order Bessel's function of the first kind. All fields (velocity, pressure etc.) are decomposed (Lamb 1932; Miles 1968; Prosperetti 1976; Menikoff *et al.* 1978; Prosperetti 1981) into a potential part indicated with subscript p and a viscous part (subscript v). The sum of the two fields are constrained to satisfy appropriate continuity conditions at the interface (discussed later). Superscripts $\mathcal{U}$ and $\mathcal{L}$ are used to indicate upper and lower fluid respectively. Thus $\Xi_p^{\mathcal{U}}$ represents the potential part of the field variable Ξ in the upper fluid and so on. The algebra is lengthy and hence only the outline is presented here along with the main results. A detailed step-by-step derivation is provided as see supplementary material available at https://doi.org/10.1017/jfm.2017.443 (Farsoiya, Mayya & Dasgupta 2017).

2.1. *IVP – potential flow*

Referring to figure 1(*a*), an axisymmetric interface between two immiscible fluids of density and viscosity $\rho^{\mathcal{L}}$, $\rho^{\mathcal{U}}$ and $\mu^{\mathcal{L}}$, $\mu^{\mathcal{U}}$ with surface tension coefficient T is represented as a standing wave

$$\eta(r, t) = a_k(t)\mathrm{J}_0(kr), \tag{2.1}$$

with $\eta(r, 0) = a_k(0)\mathrm{J}_0(kr)$, $\mathrm{J}_0(kr)$ being the zeroth-order Bessel function of the first kind. The radial dependence of all fields is chosen to be a Bessel function as these are eigenfunctions of the radial part of the Laplacian operator written in cylindrical coordinates. Our analysis is linear, retaining terms up to $O(a_k(0))$ as $a_k(0) \to 0$. We consider a stable configuration with $\rho^{\mathcal{L}} > \rho^{\mathcal{U}}$ with both fluids being radially and vertically unbounded ($0 \leqslant r \leqslant \infty$ and $-\infty \leqslant z \leqslant \infty$) (in figure 1(*b*), the boundaries are for computational purposes only, as described later). Unlike normal mode analysis which assumes an exponential dependence on time (Lamb 1932), the temporal part of all quantities are taken to be unknown functions of time (Prosperetti 1976) in

https://doi.org/10.1017/jfm.2017.443 Published online by Cambridge University Press

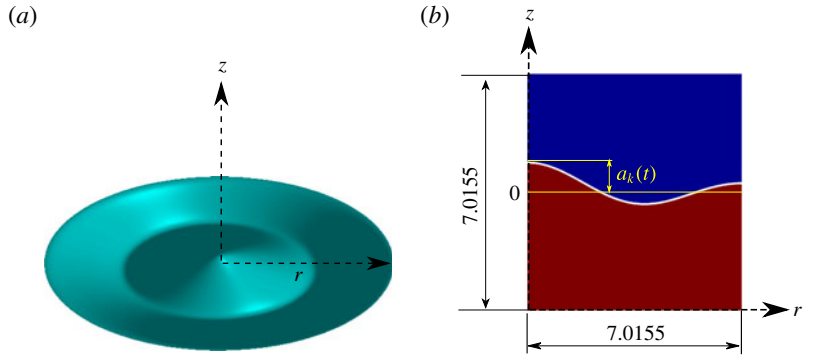


FIGURE 1. (Colour online) (*a*) The initial interface is $\eta(r,\ 0) = a_k(0)\mathrm{J}_0(kr)$. The analytical study assumes unboundedness in the radial (r) and axial (z) directions. The three-dimensional image is for visualisation purposes only. (*b*) In DNS we use symmetry boundary conditions on all computational domain boundaries. Most of the simulations are done with a domain size $[0, 7.01556] \times [0, 7.01556]$, see table 1. The left vertical boundary is the axis of symmetry. $a_k(t)$ is measured from the unperturbed interface represented by the horizontal line at level 0.

this analysis. For potential flow, we solve the axisymmetric Laplace equation in the velocity potential ϕ_p. Using variable separation in the Laplace equation, we find

$$\phi_p{}^{\mathcal{U}}(r, z, t) = F(z)\mathrm{J}_0(kr)\dot{a}_k(t), \quad \phi_p{}^{\mathcal{L}}(r, z, t) = G(z)\mathrm{J}_0(kr)\dot{a}_k(t). \tag{2.2a,b}$$

where F and G are unknown functions of z. A dot above a_k indicates differentiation with respect time. We set the time dependence of ϕ_p equal to $\dot{a}_k(t)$ anticipating the linearised kinematic boundary condition at the interface (see Farsoiya *et al.* 2017). Equations (2.2*a*,*b*) when substituted into the axisymmetric Laplace equation (Kundu & Cohen 2002), lead to equations for $F(z)$ and $G(z)$. Using the boundedness condition on $F(z)$ and $G(z)$ and the linearised kinematic boundary condition, we obtain

$$\phi_p{}^{\mathcal{U}}(r, z, t) = -k^{-1}\exp[-kz]\mathrm{J}_0(kr)\dot{a}_k(t), \quad \phi_p{}^{\mathcal{L}}(r, z, t) = k^{-1}\exp[kz]\mathrm{J}_0(kr)\dot{a}_k(t). \tag{2.3a,b}$$

The potential part of pressure in both the fluids is determined from the linearised Bernoulli equation.

$$\left.\begin{aligned} p_p^{\mathcal{L}}(r, 0, t) &= -\rho^{\mathcal{L}}\frac{\partial\phi_p{}^{\mathcal{L}}}{\partial t}\bigg|_{z=0} - \rho^{\mathcal{L}}ga_k(t)\mathrm{J}_0(kr), \\ p_p^{\mathcal{U}}(r, 0, t) &= -\rho^{\mathcal{U}}\frac{\partial\phi_p{}^{\mathcal{U}}}{\partial t}\bigg|_{z=0} - \rho^{\mathcal{U}}ga_k(t)\mathrm{J}_0(kr). \end{aligned}\right\} \tag{2.4}$$

If we wish to consider potential flow only, then continuity of pressure at the interface (in the absence of surface tension) leads to a simple harmonic oscillator equation for $a_k(t)$ with frequency $\sqrt{(\rho^{\mathcal{L}} - \rho^{\mathcal{U}})gk/(\rho^{\mathcal{L}} + \rho^{\mathcal{U}})}$.

https://doi.org/10.1017/jfm.2017.443 Published online by Cambridge University Press

2.2. *IVP – viscous flow*

Inclusion of viscous effects modifies the analysis considerably. It is known that viscous stresses are non-zero in a potential flow (Stokes 1851; Joseph 2003), and due to a jump in the viscosity across the interface, these stresses are discontinuous. In addition the tangential velocities are also discontinuous at the interface. Thus while potential flow satisfies the continuity and the Navier–Stokes equation (Joseph 2003) (also see Farsoiya *et al.* 2017), it does not satisfy the boundary conditions. In order to satisfy these, an additional velocity and pressure field is necessary. The composite velocity and pressure fields $\boldsymbol{v} = \boldsymbol{v}_p + \boldsymbol{v}_v$ and $p = p_p + p_v$ satisfy both the governing equations as well as the boundary conditions. This composite velocity field $\boldsymbol{v}$ is rotational, with vorticity being generated at the interface. In a cylindrical axisymmetric coordinate system (see figure 1), ($\boldsymbol{v} \equiv (u, v)$ with u the radial component and v the axial component of velocity.) the composite velocity and pressure fields can be written as,

$$\left.\begin{gathered} u^{\mathcal{U}} = {u_p}^{\mathcal{U}} + {u_v}^{\mathcal{U}} = \frac{\partial {\phi_p}^{\mathcal{U}}}{\partial r} + \frac{\partial {\psi_v}^{\mathcal{U}}}{\partial z}, \\ v^{\mathcal{U}} = {v_p}^{\mathcal{U}} + {v_v}^{\mathcal{U}} = \frac{\partial {\phi_p}^{\mathcal{U}}}{\partial z} - \frac{1}{r}\frac{\partial (r{\psi_v}^{\mathcal{U}})}{\partial r} \\ \text{and} \quad p = {p_p}^{\mathcal{U}} + {p_v}^{\mathcal{U}}. \end{gathered}\right\} \tag{2.5}$$

We solve the viscous fields in the streamfunction vorticity formulation by introducing the Stokes streamfunction $r\psi_v$ (Miles 1968). The relation between the streamfunction ψ_v and the azimuthal component of vorticity $\omega_\theta \equiv (\partial u_v/\partial z) - (\partial v_v/\partial r)$ is given by,

$$\frac{\partial^2 \psi_v^{\mathcal{U}}}{\partial r^2} - \frac{\psi_v^{\mathcal{U}}}{r^2} + \frac{1}{r}\frac{\partial \psi_v^{\mathcal{U}}}{\partial r} + \frac{\partial^2 {\psi_v}^{\mathcal{U}}}{\partial z^2} = {\omega_\theta}^{\mathcal{U}}. \tag{2.6}$$

The azimuthal vorticity $\omega_\theta^{\mathcal{U}}$ satisfies the diffusion equation (see Farsoiya *et al.* 2017) and using expressions for the Laplacian of a vector in cylindrical coordinates (Kundu & Cohen 2002), we obtain

$$\frac{\partial {\omega_\theta}^{\mathcal{U}}}{\partial t} = \nu^{\mathcal{U}} \left(\frac{\partial^2 {\omega_\theta}^{\mathcal{L}}}{\partial r^2} - \frac{{\omega_\theta}^{\mathcal{U}}}{r^2} + \frac{1}{r}\frac{\partial {\omega_\theta}^{\mathcal{U}}}{\partial r} + \frac{\partial^2 {\omega_\theta}^{\mathcal{U}}}{\partial z^2} \right). \tag{2.7}$$

We set,

$$\omega_\theta^{\mathcal{U}}(r, z, t) = \Omega^{\mathcal{U}}(z, t)\mathrm{J}_1(kr), \quad \psi_v^{\mathcal{U}}(r, z, t) = \Psi^{\mathcal{U}}(z, t)\mathrm{J}_1(kr), \tag{2.8a,b}$$

the radial part of all quantities being set equal to $\mathrm{J}_1(kr)$, (the first-order Bessel function of the first kind) to be consistent with the structure of (2.7) and other boundary conditions. Substituting (2.8) in (2.7) and (2.6) and using the equation governing $\mathrm{J}_1(kr)$, we obtain

$$\frac{\partial \Omega^{\mathcal{U}}}{\partial t} = \nu^{\mathcal{U}} \left(\frac{\partial^2 \Omega^{\mathcal{U}}}{\partial z^2} - k^2 \Omega^{\mathcal{U}} \right), \quad \frac{\partial^2 \Psi^{\mathcal{U}}}{\partial z^2} - k^2 \Psi^{\mathcal{U}} = \Omega^{\mathcal{U}}. \tag{2.9a,b}$$

Equations (2.9) are identical to the ones derived by Prosperetti (1981) in planar geometry. The equations for $\Omega^{\mathcal{U}}$ and $\Psi^{\mathcal{U}}$ (along with an analogous set for $\Omega^{\mathcal{L}}$

https://doi.org/10.1017/jfm.2017.443 Published online by Cambridge University Press

and $\Psi^{\mathcal{L}}$) are to be solved as initial boundary value problems with the following boundary and initial conditions for both fluids (Prosperetti 1981).

$$\Omega^{\mathcal{U}}(z,0)=\Omega^{\mathcal{L}}(z,0)=\Psi^{\mathcal{U}}(z,0)=\Psi^{\mathcal{L}}(z,0)=0, \tag{2.10}$$

$$\Psi^{\mathcal{U}}(\infty,t)=\Omega^{\mathcal{U}}(\infty,0)=0, \quad \Psi^{\mathcal{L}}(-\infty,t)=\Omega^{\mathcal{L}}(-\infty,0)=0 \tag{2.11a,b}$$

$$\mu^{\mathcal{U}}\Omega^{\mathcal{U}}(0,t)-\mu^{\mathcal{L}}\Omega^{\mathcal{L}}(0,t)=-2k(\mu^{\mathcal{L}}-\mu^{\mathcal{U}})\dot{a}_k(t), \tag{2.12}$$

$$\left(\frac{\partial\Psi^{\mathcal{L}}}{\partial z}-\frac{\partial\Psi^{\mathcal{U}}}{\partial z}\right)\Bigg|_{z=0,t}=2\dot{a}_k(t), \tag{2.13}$$

$$\Psi^{\mathcal{U}}(0,t)=\Psi^{\mathcal{L}}(0,t)=0. \tag{2.14}$$

These boundary conditions arise from boundedness at $\pm\infty$, continuity of tangential stresses and tangential velocities and the kinematic boundary condition at the linearised interface (see Farsoiya *et al.* (2017) for detailed derivation of these) respectively.

We have four equations *viz.* equations (2.9) (and their counterpart for the lower fluid) in the four unknowns $\Omega^{\mathcal{U}}$, $\Psi^{\mathcal{U}}$, $\Omega^{\mathcal{L}}$ and $\Psi^{\mathcal{L}}$ and these can be solved with boundary and initial conditions (2.10)–(2.14). However, there is an additional unknown $a_k(t)$ in these equations and we can express the four unknowns in terms of $a_k(t)$. The yet unused normal stress boundary condition provides an additional equation for determining $a_k(t)$ and thus there is a closed system of equations. Equations (2.9) and the corresponding ones for the upper fluid are easily solved in the Laplace transformed s domain to obtain (see Farsoiya *et al.* (2017) for the algebra)

$$\left.\begin{gathered}\tilde{\Omega}^{\mathcal{U}}(z,s)=\tilde{A}^{\mathcal{U}}(s)\exp[-z\lambda_{\mathcal{U}}], \quad \tilde{\Omega}^{\mathcal{L}}(z,s)=\tilde{A}^{\mathcal{L}}(s)\exp[z\lambda_{\mathcal{L}}]\\ \tilde{\Psi}^{\mathcal{U}}(z,s)=\frac{\tilde{A}^{\mathcal{U}}(s)}{\lambda_{\mathcal{U}}^2-k^2}(\exp[-z\lambda_{\mathcal{U}}]-\exp[-kz]),\\ \tilde{\Psi}^{\mathcal{L}}(z,s)=\frac{\tilde{A}^{\mathcal{L}}(s)}{\lambda_{\mathcal{L}}^2-k^2}(\exp[z\lambda_{\mathcal{L}}]-\exp[kz]),\end{gathered}\right\} \tag{2.15}$$

where variables with tilde on top are in the Laplace domain, $\lambda_{\mathcal{L}}\equiv\sqrt{k^2+s/\nu^{\mathcal{L}}}$ etc. (Prosperetti 1981) and $\tilde{A}^{\mathcal{L}}(s)$, $\tilde{A}^{\mathcal{U}}(s)$ are partial integration constants. Expressions for $\tilde{A}^{\mathcal{L}}(s)$, $\tilde{A}^{\mathcal{U}}(s)$ are provided in Farsoiya *et al.* (2017). In order to obtain an expression for the viscous contribution to pressure, we can integrate the axial momentum equation along the z direction. In Laplace domain, the expressions are (see algebra in Farsoiya *et al.* 2017),

$$\tilde{p_v}^{\mathcal{L}}(r,z,s)=-\mu^{\mathcal{L}}\tilde{A}^{\mathcal{L}}(s)\mathrm{J}_0(kr)\exp[kz], \quad \tilde{p_v}^{\mathcal{U}}(r,z,s)=\mu^{\mathcal{U}}\tilde{A}^{\mathcal{U}}(s)\mathrm{J}_0(kr)\exp[-kz]. \tag{2.16a,b}$$

In order to obtain an equation for $\tilde{a}_k(s)$, we use the Laplace transform of the normal stress jump condition (Bush 2013),

$$\sigma_{zz}^{\mathcal{U}}(r,0,t)-\sigma_{zz}^{\mathcal{L}}(r,0,t)=T(\boldsymbol{\nabla}\cdot\boldsymbol{n}), \tag{2.17}$$

where $\boldsymbol{n}$ is the local unit normal to an axisymmetric interface $z=\eta(r,t)=a_k(t)\mathrm{J}_0(kr)$ and T is the surface tension coefficient. Using the Newtonian constitutive relation in (2.17), it is shown in Farsoiya *et al.* (2017) that we obtain the following expression for $\tilde{a}_k(s)$

https://doi.org/10.1017/jfm.2017.443 Published online by Cambridge University Press

$$\tilde{a}_k(s) = \frac{\left[s + \dfrac{1}{\rho^{\mathcal{U}} + \rho^{\mathcal{L}}}\left\{2k^2(\mu^{\mathcal{U}} + \mu^{\mathcal{L}}) + k(\mu^{\mathcal{U}}\zeta + \mu^{\mathcal{L}}\xi) - 2k^2\left(\dfrac{\mu^{\mathcal{U}}\zeta}{\lambda_{\mathcal{U}} + k} + \dfrac{\mu^{\mathcal{L}}\xi}{\lambda_{\mathcal{L}} + k}\right)\right\}\right]}{s^2 + \dfrac{1}{\rho^{\mathcal{U}} + \rho^{\mathcal{L}}}\left\{2k^2(\mu^{\mathcal{U}} + \mu^{\mathcal{L}}) + k(\mu^{\mathcal{U}}\zeta + \mu^{\mathcal{L}}\xi) - 2k^2\left(\dfrac{\mu^{\mathcal{U}}\zeta}{\lambda_{\mathcal{U}} + k} + \dfrac{\mu^{\mathcal{L}}\xi}{\lambda_{\mathcal{L}} + k}\right)\right\}s + \omega_0^2} a_k(0), \tag{2.18}$$

where $\omega_0^2 = gk(\rho^{\mathcal{L}} - \rho^{\mathcal{U}}/\rho^{\mathcal{L}} + \rho^{\mathcal{U}}) + Tk^3/\rho^{\mathcal{L}} + \rho^{\mathcal{U}}$ and $\zeta(s)$ and $\xi(s)$ are given by

$$\zeta(s) \equiv \frac{2(k + \lambda_{\mathcal{U}})(\mu^{\mathcal{U}}k + \mu^{\mathcal{L}}\lambda_{\mathcal{L}})}{\mu^{\mathcal{L}}(k + \lambda_{\mathcal{L}}) + \mu^{\mathcal{U}}(k + \lambda_{\mathcal{U}})}, \quad \xi(s) \equiv \frac{2(k + \lambda_{\mathcal{L}})(\mu^{\mathcal{L}}k + \mu^{\mathcal{U}}\lambda_{\mathcal{U}})}{\mu^{\mathcal{L}}(k + \lambda_{\mathcal{L}}) + \mu^{\mathcal{U}}(k + \lambda_{\mathcal{U}})}. \tag{2.19a,b}$$

Equations (2.15), (2.16) and (2.18) are not analytically invertible in the most general case (Prosperetti 1981). We invert these numerically using the open source MATLAB (2015) code by McClure (2016) (based on the algorithm by Abate & Whitt (2006)), when comparing with results from Navier–Stokes simulations in the next section. The numerical inversion code has been benchmarked in house by comparing its output against known Laplace inversions.

Analytical expressions for $a_k(t)$ are obtainable for the cases when both fluids have equal kinematic viscosity (Chandrasekhar 1961; Menikoff *et al.* 1978; Prosperetti 1981). In this limit (2.18) can be inverted to obtain (see Farsoiya *et al.* (2017) for detailed algebra)

$$\frac{a_k(t)}{a_k(0)} = \frac{4(\nu k^2)^2(1 - 4\beta)}{8(\nu k^2)^2(1 - 4\beta) + \omega_0^2}\mathrm{Erfc}\left(\sqrt{\nu k^2 t}\right) + \sum_{i=1}^{4}\frac{\hat{A}_i\hat{h}_i\omega_0^2\exp[(\hat{h}_i^2 - \nu k^2)t]\mathrm{Erfc}\,(\hat{h}_i\sqrt{t})}{\nu k^2 - \hat{h}_i^2}, \tag{2.20}$$

where $\hat{h}_i$ are the distinct roots (for over-/under-damped motion) of

$$\hat{P}(\hat{h}) = \hat{h}^4 - 4(\nu k^2)^{1/2}\beta\hat{h}^3 + 2(\nu k^2)(1 - 6\beta)\hat{h}^2 + 4(\nu k^2)^{3/2}(1 - 3\beta)\hat{h} + (\nu k^2)^2(1 - 4\beta) + \omega_0^2, \tag{2.21}$$

and $\hat{A}_i$ is the partial fraction decomposition $\hat{P}(\hat{h})^{-1} = \sum_{i=1}^{4}\hat{A}_i(\hat{h} - \hat{h}_i)^{-1}$. Note that $\beta \equiv (\rho^{\mathcal{U}}\rho^{\mathcal{L}}/(\rho^{\mathcal{L}} + \rho^{\mathcal{U}})^2)$. This is the same expression obtained earlier in planar geometry by Prosperetti (1976). Analytical expressions for vorticity and pressure can also be obtained. For the lower fluid (see Farsoiya *et al.* 2017),

$$\omega_\theta{}^{\mathcal{L}}(r, z, t) = \left(\frac{\mathrm{J}_1(kr)\nu^{-1/2}}{\rho^{\mathcal{U}} + \rho^{\mathcal{L}}}\right)\left[\int_0^t \mathrm{d}m\,\frac{\dot{a}_k(m)\exp\left[-\left(\nu k^2(t - m) + \dfrac{z^2}{4\nu(t - m)}\right)\right]}{\sqrt{\pi(t - m)^3}}\right.$$
$$\left. \times \left(-zk\rho^{\mathcal{L}} + \frac{\rho^{\mathcal{U}}}{2}H_2\left(\frac{-z}{2\sqrt{\nu(t - m)}}\right)\right)\right], \tag{2.22}$$

where $H_2(x) \equiv 4x^2 - 2$ is the Hermite polynomial (Abramowitz & Segun 1970). Similarly we can obtain an expression for pressure in the lower fluid (see Farsoiya *et al.* 2017),

$$\frac{p_v{}^{\mathcal{L}}(r, z, t)}{\mu^{\mathcal{L}}\omega_0} = -\mathrm{J}_0(kr)\exp[kz]\left[\frac{2\rho^{\mathcal{L}}k\omega_0^{-1}}{\rho^{\mathcal{L}} + \rho^{\mathcal{U}}}\dot{a}_k(t) - \frac{2\rho^{\mathcal{U}}a_k(0)\omega_0^{1/2}\nu^{-1/2}}{\rho^{\mathcal{L}} + \rho^{\mathcal{U}}}\exp[-\nu k^2 t]\right.$$
$$\left. \times \sum_{i=1}^{4}\hat{B}_i\hat{h}_i\omega_0^{1/2}\exp[\hat{h}_i^2 t]\mathrm{Erfc}\,[\hat{h}_i\sqrt{t}]\right], \tag{2.23}$$

https://doi.org/10.1017/jfm.2017.443 Published online by Cambridge University Press

where $\hat{h}_i$ are the roots of the equation $\hat{P}(\hat{h}) = 0$ and the values of $\hat{B}_i$ are obtained from the partial fraction decomposition $-\hat{h}\hat{P}(\hat{h})^{-1} = \sum_{i=1}^{4} \hat{B}_i(\hat{h} - \hat{h}_i)^{-1}$. Note that the expressions for vorticity and pressure provided here are new and have not been previously reported in the literature.

3. Normal mode approximation

We have shown in the previous section that the expression for $a_k(t)$ is the same in planar and cylindrical axisymmetric geometries. It has been shown earlier by Prosperetti (1981) that the normal mode dispersion relation can be recovered from the expression for $\tilde{a}_k(s)$. Since the expression of $\tilde{a}_k(s)$ is the same in planar as well as axisymmetric geometries, we can expect that the dispersion relations would also be the same. Such a dispersion relation in planar geometry involving inertia and viscosity in both fluids is provided in Chandrasekhar (1961) and reads, (while adopting the planar dispersion relation in Chandrasekhar (1961) for our axisymmetric case below, we assume that all fields are proportional to $\exp[nt]$ and that the wavenumber dependence k comes from $\mathrm{J}_0(kr)$ or $\mathrm{J}_1(kr)$)

$$\begin{aligned}
&-\left\{\frac{gk}{n^2}\left[(\alpha^{\mathcal{L}} - \alpha^{\mathcal{U}}) + \frac{k^2 T}{g(\rho^{\mathcal{L}} + \rho^{\mathcal{U}})}\right] + 1\right\}(\alpha^{\mathcal{U}} q^{\mathcal{L}} + \alpha^{\mathcal{L}} q^{\mathcal{U}} - k) - 4k\alpha^{\mathcal{L}}\alpha^{\mathcal{U}} \\
&+ \frac{4k^2}{n}(\alpha^{\mathcal{L}}\nu^{\mathcal{L}} - \alpha^{\mathcal{U}}\nu^{\mathcal{U}})\{(\alpha^{\mathcal{U}} q^{\mathcal{L}} - \alpha^{\mathcal{L}} q^{\mathcal{U}}) + k(\alpha^{\mathcal{L}} - \alpha^{\mathcal{U}})\} \\
&+ \frac{4k^3}{n^2}(\alpha^{\mathcal{L}}\nu^{\mathcal{L}} - \alpha^{\mathcal{U}}\nu^{\mathcal{U}})^2(q^{\mathcal{L}} - k)(q^{\mathcal{U}} - k) = 0, \qquad (3.1)
\end{aligned}$$

where

$$\alpha^{\mathcal{L}} \equiv \frac{\rho^{\mathcal{L}}}{\rho^{\mathcal{L}} + \rho^{\mathcal{U}}}, \quad \alpha^{\mathcal{U}} \equiv \frac{\rho^{\mathcal{U}}}{\rho^{\mathcal{L}} + \rho^{\mathcal{U}}}, \quad q^{\mathcal{L}} \equiv \sqrt{k^2 + \frac{n}{\nu^{\mathcal{L}}}}, \quad q^{\mathcal{U}} \equiv \sqrt{k^2 + \frac{n}{\nu^{\mathcal{U}}}}. \quad (3.2a\text{–}d)$$

From the normal mode approximation, the expression for $a_k(t)$ is (for $\dot{a}_k(0) = 0$),

$$a_k(t) = \frac{a_k(0)}{n_1 - n_2}[n_1 \mathrm{e}^{n_2 t} - n_2 \mathrm{e}^{n_1 t}] \quad \text{for } n_1 \neq n_2, \qquad (3.3)$$

and n_1 and n_2 are the two roots of equation (3.1). Equation (3.1) is solved in Mathematica (Wolfram Research Inc. 2010) to determine the roots. For over-damped oscillations n_1 and n_2 are real while in the under-damped case they occur as a complex conjugate pair. In order to test the validity of the linearised IVP solution in (2.20) and the normal mode solution in (3.3), we turn to numerical simulations.

4. DNS

We solve the axisymmetric incompressible Navier–Stokes equations using an open source code Basilisk (Popinet 2014). Basilisk is a successor to the popular open source solver Gerris (Popinet 2003) and has been extensively benchmarked on a wide range of problems involving interfaces (Popinet 2015; Beetham *et al.* 2016). It uses the finite volume method and the Bell–Colella–Glaz (Bell, Colella & Glaz 1989) advection scheme. A semi-implicit scheme is used to evaluate the velocity and pressure fields. For interface capturing, the volume of fluid method (Hirt &

https://doi.org/10.1017/jfm.2017.443 Published online by Cambridge University Press

Nichols 1981) is implemented with continuum surface force model for surface tension (Brackbill, Kothe & Zemach 1992).

$$\partial_t \boldsymbol{u} + \boldsymbol{\nabla}\cdot(\boldsymbol{u}\otimes\boldsymbol{u}) = \frac{1}{\rho}\left[-\boldsymbol{\nabla}p + \boldsymbol{\nabla}\cdot\mu(\boldsymbol{\nabla}\boldsymbol{u} + \boldsymbol{\nabla}\boldsymbol{u}^{\mathrm{T}})\right] + \boldsymbol{g} + T\kappa\delta_s\boldsymbol{n} \tag{4.1}$$

$$\boldsymbol{\nabla}\cdot\boldsymbol{u} = 0, \quad \partial_t f + \boldsymbol{\nabla}\cdot(f\boldsymbol{u}) = 0, \tag{4.2a,b}$$

where $\boldsymbol{u}$, p, T, κ and f are velocity, pressure, surface tension coefficient, curvature and volume fraction fields respectively. Referring to figure 1(*b*), the interface is initiated as $a_k(0)\mathrm{J}_0(kr)$. The domain extends up to the third extrema of J_0 along the radial direction although the results are independent of this. The vertical domain size was arrived at by checking for domain size independence in the vertical direction. Since our theoretical results are for axially and radially unbounded domain, we impose symmetry boundary conditions on all four sides of the computational domain in figure 1(*b*). This implies zero normal velocities and Neumann conditions on tangential velocity, pressure and volume fractions on boundaries. In our Basilisk input script file, we approximate $\mathrm{J}_0(kr)$ by numerical integration using the following definition,

$$\mathrm{J}_0(kr) = \frac{1}{\pi}\int_0^{\pi} \cos(kr\sin(l))\,\mathrm{d}l. \tag{4.3}$$

With $a_0 \equiv a_k(0)$, the non-dimensional numbers which govern the problem are non-dimensional amplitude $\epsilon \equiv a_0 k$, density ratio $\rho_r \equiv \rho^{\mathcal{L}}/\rho^{\mathcal{U}}$, viscosity ratio $\mu_r \equiv \mu^{\mathcal{L}}/\mu^{\mathcal{U}}$, Laplace number $La \equiv T\rho^{\mathcal{U}}/((\mu^{\mathcal{U}})^2 k)$ and Galilei number $Ga \equiv g(\rho^{\mathcal{U}})^2/((\mu^{\mathcal{U}})^2 k^3)$. The parametric space is large and the simulations carried out for the present study are listed in table 1. The choice for the range of values for La and Ga arise from the fact that for air–water combination, these numbers are very large e.g. for air as the upper fluid and water as lower fluid in the Earth's gravitational field in CGS units, $T = 72$, $\rho^{\mathcal{U}} = 1.5\times10^{-3}$, $\rho^{\mathcal{L}} = 1$, $\mu^{\mathcal{U}} = 1.8\times10^{-4}$, $k = 1$, $g = 981$ leads to $Ga = 6.81\times10^4$ and $La = 3.33\times10^6$. While most of the simulations are done with a domain size of $[0, 7.0155]\times[0, 7.0155]$, for others (table 1) larger domains were necessary (see § 5).

5. Results and discussion

A comparison of the normal mode approximation (3.3), the IVP solution in (2.18) inverted numerically (McClure 2016) and results from DNS are presented in figure 2. Note that $\tau \equiv t\omega_0$ with $\omega_0^2 \equiv gk(\rho^{\mathcal{L}} - \rho^{\mathcal{U}}/\rho^{\mathcal{L}} + \rho^{\mathcal{U}}) + (Tk^3/\rho^{\mathcal{U}} + \rho^{\mathcal{L}})$. In the case of simulations, the location of the interface is tracked at the axis of symmetry i.e. $r = 0$ (although any other radial location also shows the same trend). Figure 2(*a,b*) correspond to under-damped oscillations while figure 2(*c,d*) are for over-damped oscillations. The excellent agreement between the solution to the IVP and the Navier–Stokes simulation is apparent. It is also seen that while normal mode is a good approximation to the IVP solution (2.20) for low values of μ_r, the difference between the two increases at higher values of viscosity ratio, especially at intermediate times. Figure 3(*a*) validates the analytical prediction made in § 2. For sufficiently small amplitudes, our axisymmetric DNS results agree very well with the planar DNS results obtained from Denner *et al.* (2017*a*) (rows #42 and #113 in data provided in Denner, Paré & Zaleski (2017*b*). The axisymmetric wavenumber k of the Bessel mode was chosen to be the same as the planar wavenumber in Denner *et al.* (2017*b*)). This comparison is done for a pure capillary wave with zero gravity. At larger amplitudes, the axisymmetric simulation shows deviations from the planar one. In agreement with the earlier observations of Denner *et al.* (2017*a*),

https://doi.org/10.1017/jfm.2017.443 Published online by Cambridge University Press

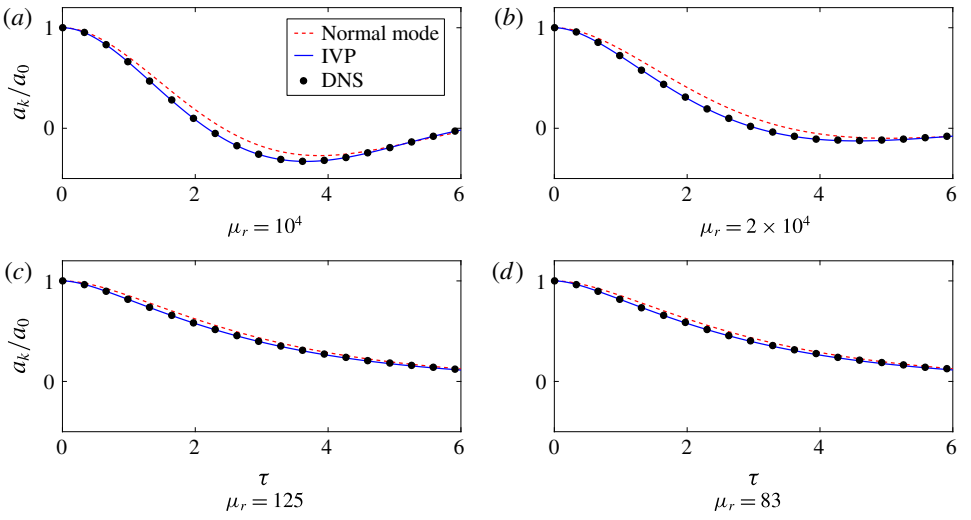


FIGURE 2. (Colour online) Comparisons between normal mode approximation, initial value problem and Navier–Stokes simulation for cases (*a*) 14, (*b*) 15, (*c*) 29 and (*d*) 30 in table 1.

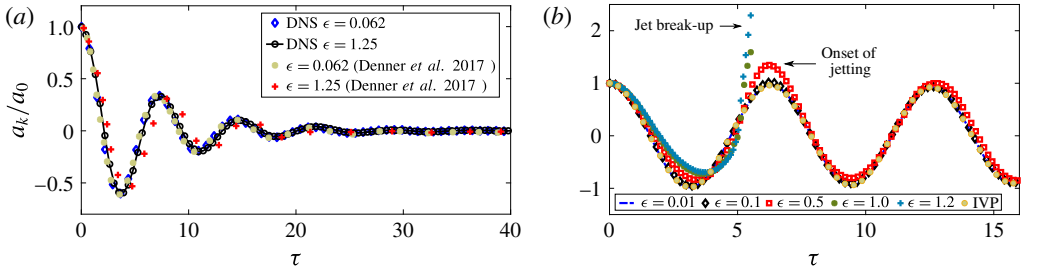


FIGURE 3. (Colour online) (*a*) Cases 31, 32 in table 1 – comparison of axisymmetric DNS simulations with planar DNS simulations of Denner *et al.* (2017*a*) for small- and large-amplitude, pure capillary oscillations. (*b*) Effect of increase of ϵ for cases 1, 2, 3, 4 and 5 in table 1. Note the onset of 'jetting' and subsequent break-up as ϵ is increased.

increasing the amplitude decreases the frequency (Prosperetti 1980) of oscillation in the axisymmetric case as well (see Becker, Hiller & Kowalewski (1991) and Trinh & Wang (1982) for analogous observations for large-amplitude droplet oscillations). Figure 3(*b*) shows the effect of increasing ϵ on amplitude $a_k(t)$ as a function of time. For $\epsilon = 0.01$ and 0.1, the IVP solution given by (2.20) is an excellent approximation. For ϵ larger than 0.5, there are marked deviations due to nonlinear effects. For increasing values of ϵ, the interface at the axis of symmetry starts rising to a height greater than $a_k(0)$. We call this phenomena 'jetting'. Note that for pure capillary waves in figure 3(*a*), one does not observe jetting at the non-dimensional parametric values reported in Denner *et al.* (2017*a*). While observations of jetting (Worthington jets) have been reported earlier in the context of standing waves hitting a wall (Longuet-Higgins 2001), standing waves generated through forced oscillations (Zeff *et al.* 2000), droplet impact (Bartolo, Josserand & Bonn 2006) and water entry of axisymmetric objects (Gekle & Gordillo 2010), observation of jetting in purely free

https://doi.org/10.1017/jfm.2017.443 Published online by Cambridge University Press

Remarks	Case	ϵ	ρ_r	μ_r	La	Ga	Domain	Grid
ϵ	1	0.01	100	100	10^6	10^5	L_1^2	512^2
	2	0.1	do	do	do	do	do	do
	3	0.5	do	do	do	do	do	do
	4	1.0	do	do	do	do	do	do
	5	1.2	do	do	do	do	do	do
	6	1.5	do	do	do	do	L_2^2	1024^2
ρ_r	7	0.01	1	do	do	do	L_1^2	512^2
	8	do	10	do	do	do	do	do
	9	do	1000	do	do	do	do	do
μ_r	10	do	100	0.1	do	do	do	do
	11	do	do	1	do	do	do	do
	12	do	do	10	do	do	do	do
	13	do	do	10^3	do	do	do	do
	14	do	do	10^4	do	do	do	do
	15	do	do	2×10^4	do	do	do	do
	16	do	do	5×10^4	do	do	do	do
	17	do	do	10^5	do	do	do	do
La	18	do	do	10^2	5.0×10^6	do	do	do
	19	do	do	do	1.0×10^7	do	do	do
	20	do	do	do	1.5×10^7	do	do	do
Ga	21	do	do	do	10^6	5.0×10^5	do	do
	22	do	do	do	do	1.0×10^6	do	do
	23	do	do	do	do	1.5×10^6	do	do
Hankel	24	0.5	do	do	do	10^5	L_3^2	1024^2
Transform	25	1.5	do	do	do	do	do	do
	26	3.5	do	do	do	do	do	do
Pinch off	27	1.1	10^3	10^3	7.2×10^6	9.81×10^4	L_2^2	do
	28	1.1	10^3	1.5×10^3	7.2×10^6	9.81×10^4	do	do
Normal	29	0.01	10^2	125	6.25	0.625	L_1^2	512^2
mode[a]	30	0.01	do	83	2.78	0.278	do	512^2
Comparison with	31	0.062	1	1	126	0	L_4^2	256^2
Denner *et al.* (2017*a*)	32	1.25	do	do	do	do	do	do
ϵ		ρ_r	μ_r	La	Ga	L_1	L_2	L_3	L_4
$a_0 k$		$\frac{\rho^{\mathcal{L}}}{\rho^{\mathcal{U}}}$	$\frac{\mu^{\mathcal{L}}}{\mu^{\mathcal{U}}}$	$\frac{T\rho^{\mathcal{U}}}{(\mu^{\mathcal{U}})^2 k}$	$\frac{g(\rho^{\mathcal{U}})^2}{(\mu^{\mathcal{U}})^2 k^3}$	7.0155	16.4706	35.3323	8.66×10^6

TABLE 1. DNS Parameters.

[a]Cases 14 and 15 are also use for normal mode comparison with DNS.
The bottom row of the table lists the simulation parameters and their formulae/values. Simulations having square domain of size L_1, L_2, L_3 and L_4 are performed. The values for these are in centimetres and $L_1 \times L_1 \equiv L_1^2$ etc.

oscillations is reported here for the first time. In figure 3(*b*), as ϵ is increased further up to a value of 1.2, a droplet pinches off from the jet. This is referred to as jet break-up and droplet pinch off (see Leal (2007), p. 83 for discussion of a capillary mechanism of end pinch off in cylindrical threads).

https://doi.org/10.1017/jfm.2017.443 Published online by Cambridge University Press

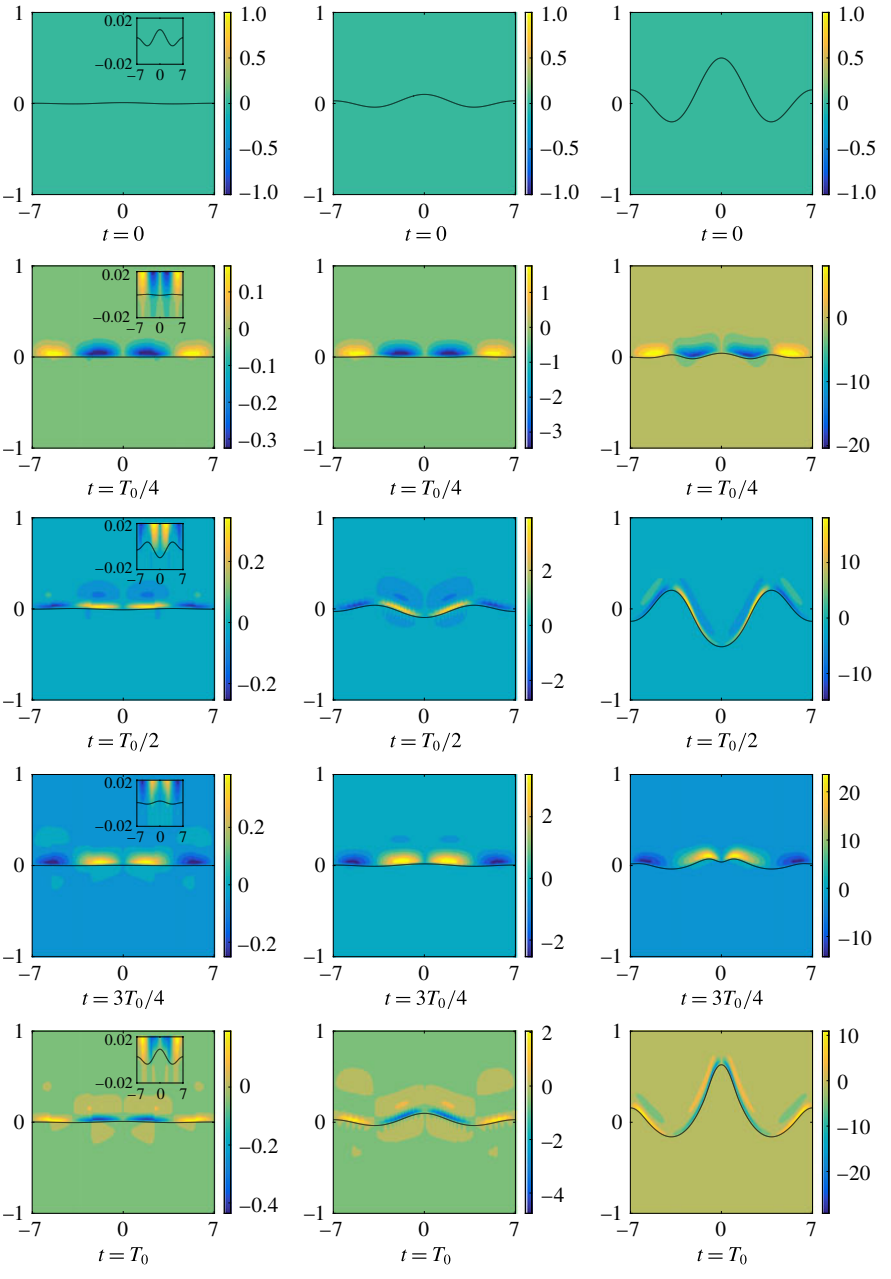


FIGURE 4. (Colour online) Interface with vorticity contours for cases 1, 2 and 3 in table 1. For visualisation, the interface is mirrored about the axis of symmetry. From left to right $\epsilon = 0.01, 0.1$ and 0.5 respectively for the columns. Note the onset of 'jetting' in the third column.

The effect of increasing ϵ is visualised as a collage in figures 4 and 5. Both these figures are to be read along columns. Each column shows the interface evolving in time for a particular value of ϵ, all other non-dimensional parameters being the same.

https://doi.org/10.1017/jfm.2017.443 Published online by Cambridge University Press

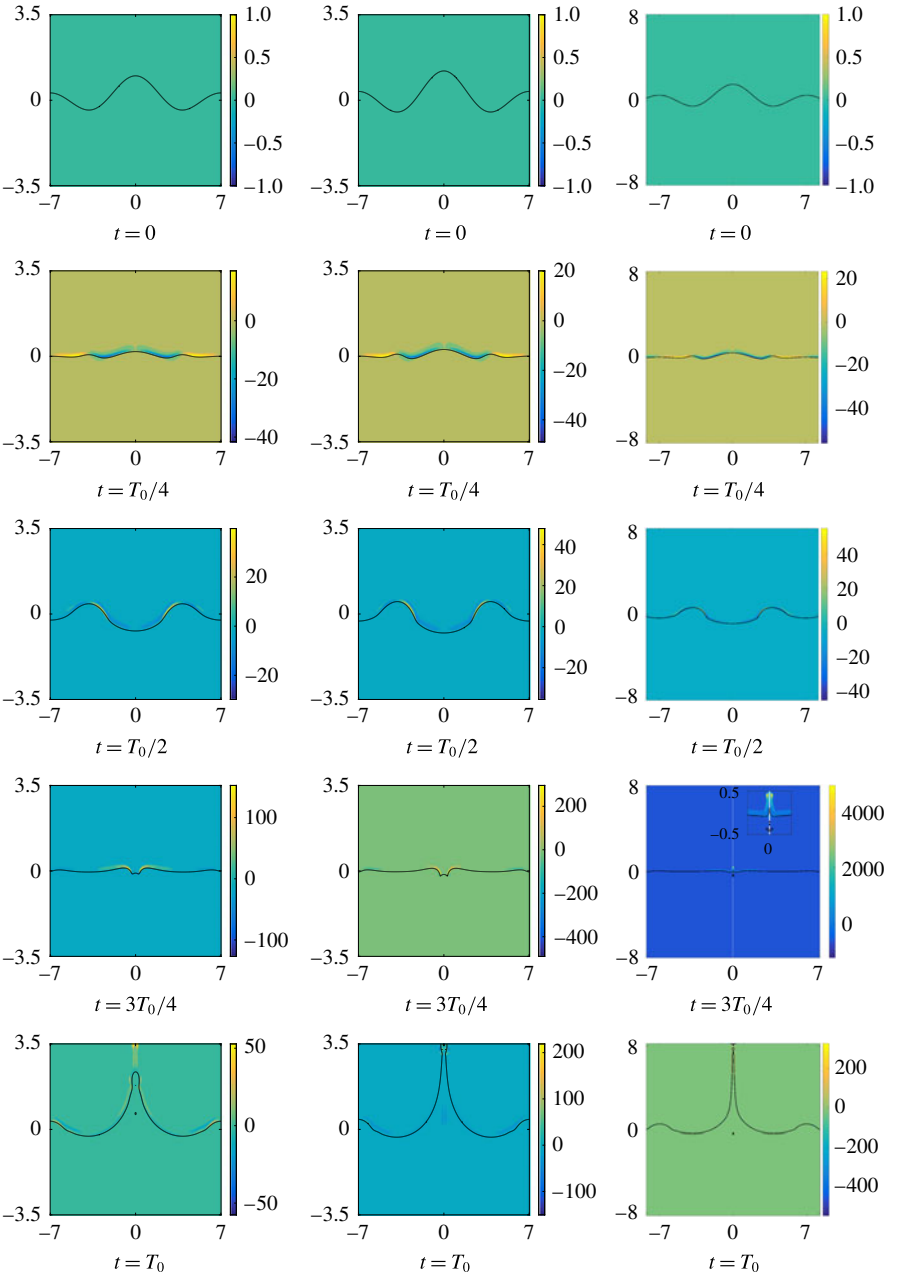


FIGURE 5. (Colour online) Interface with vorticity contours for cases 4, 5 and 6 in table 1. From left to right $\epsilon = 1.0$, 1.2 and 1.5 respectively for the columns. Due to strong jetting in case of $\epsilon = 1.5$, the domain size had to be enlarged. Domain size independence of results has been verified for all cases.

The background colour contours represent the vorticity field. It is clearly seen from figure 4 that most of the vorticity is limited to a thin region around the interface, with the maximum value of vorticity being an increasing function of ϵ. It is also

https://doi.org/10.1017/jfm.2017.443 Published online by Cambridge University Press

seen that the peak value of vorticity (magnitude) seems to concentrate in the lighter fluid (see Tripathi, Sahu & Govindarajan (2014) and Dixit & Govindarajan (2010) for related analysis of this). Further the magnitude of the vorticity fields is an increasing function of ϵ as seen from the increasing scale of the colour bars. Impending droplet pinch off is clearly visible in the last image of all three columns in figure 5. For ϵ larger than 0.5, nonlinear effects are clearly visible e.g. the instantaneous shape of the interface at the row corresponding to $t = T_0/2$ ($T_0 \equiv 2\pi/\omega_0$) in all the columns in figure 5 is very different from $\mathrm{J}_0(kr)$, the assumption in (2.1). However at the end of one oscillation (for $\epsilon \leqslant 0.5$), the interface returns to a shape which is approximately $\mathrm{J}_0(kr)$ again, cf. last row of figure 4. In figure 6, we compare the IVP predictions of the vorticity field from (2.22) (see Farsoiya *et al.* (2017) for the expression for the upper fluid). Equation (2.22) and the corresponding equation for the upper fluid was numerically integrated in Mathematica (Wolfram Research Inc. 2010) using the subroutine NIntegrate. Note that $\hat{\omega} \equiv \omega/\mathrm{J}_1(kr)$. The left column for $\epsilon = 0.01$ shows excellent agreement with DNS results in both the fluids. The collapse of the curves at different radial locations $r = 1, 3$ shows the accuracy of the linear estimation. Note that the extrema of vorticity for the upper and lower fluid are slightly above and below the linearised interface $z = 0$. In figure 6, as ϵ is increased ($\epsilon = 0.5$), systematic deviations are seen from linear predictions. While the shapes of the vorticity profiles at different radial locations appear broadly the same, a collapse of these profiles by scaling with $\mathrm{J}_1(kr)$ no longer appears possible, hinting at the appearance of higher modes. It is also seen that there is a vorticity jump at the interface. The inset in the first column in figure 4 shows this jump as we cross the interface. This is consistent with the linearised predictions from (2.12) reflecting the fact that the interface acts as a source of vorticity (Brøns *et al.* 2014). The vorticity jump at the interface can however be minimised by choosing the viscosity ratio $\mu_r = 1$. To see this, we rewrite (2.12) as,

$$\Omega^{\mathcal{U}}(0, t) = \mu_r \Omega^{\mathcal{L}}(0, t) - 2k(\mu_r - 1)\dot{a}_k(t). \tag{5.1}$$

It is clear that for $\mu_r = 1$, the vorticity jump between the upper and lower fluid at the interface goes to zero i.e. $\Omega^{\mathcal{L}}(0, t) = \Omega^{\mathcal{U}}(0, t)$. This prediction is borne out by simulations. In the insets of figure 7(*a–c*) as we make $\mu_r = 1$ (figure 7*b*), the difference between the colour of vorticity contours reduces as we cross the interface, although it does not become zero. Note that (5.1) predicts that for $\mu_r \neq 1$, the vorticity jump across the interface depends both on viscosity ratio as well as the density ratio, through $\dot{a}_k(t)$. It should be remembered that (5.1) is a linearised prediction applicable to the vorticity values immediately above and below the interface only.

Figure 8 shows the effect of variation of parameters on under-damped oscillations. Figure 8(*a*) shows the influence of Galilei number. At larger values of *Ga*, one can collapse all the curves by scaling t with ω_0. However this collapse fails as one reduces the value of *Ga*. Note however that for surface tension driven, pure capillary oscillations a collapse is possible using the time scale proposed in Denner (2016). This is demonstrated in Farsoiya *et al.* (2017). Increasing the viscosity ratio in figure 8(*b*) increases the damping but the time period remains relatively unaffected. Increasing the density ratio in figure 8(*c*) has an effect both on the time period (as one can estimate from the inviscid dispersion relation) as well as on the damping. Note that for $\rho_r = 1$, the effect of gravity drops out and these become under-damped pure capillary oscillations. For $\rho_r = 1000$ ($\mu_r = 100$), the inviscid-irrotational approximation of a undamped harmonic oscillator with frequency ω_0 is an excellent approximation for the first few oscillations. The effect of change of Laplace number is shown in figure 8(*d*) where we see some damping but hardly any change in the time period.

https://doi.org/10.1017/jfm.2017.443 Published online by Cambridge University Press

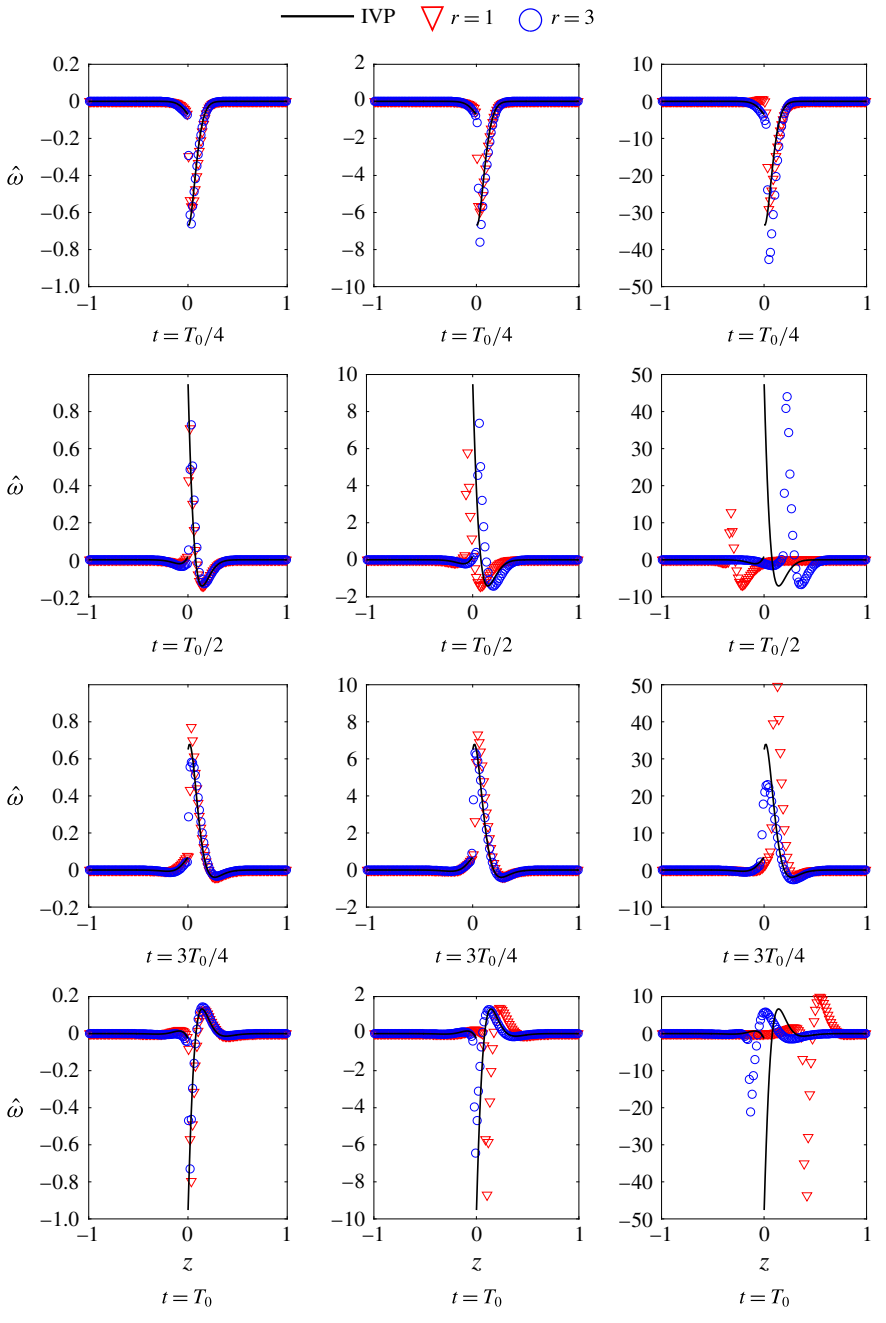


FIGURE 6. (Colour online) Vorticity $\hat{\omega} \equiv \omega_\theta / \mathrm{J}_1(kr)$ versus z for cases 1, 2 and 3 in table 1. From left to right, the columns are for $\epsilon = 0.01, 0.1$ and 0.5 respectively.

In order to understand the modal structure of the interface and study the emergence of new modes due to nonlinearity, we use Hankel transform of the interface defined by the following

https://doi.org/10.1017/jfm.2017.443 Published online by Cambridge University Press

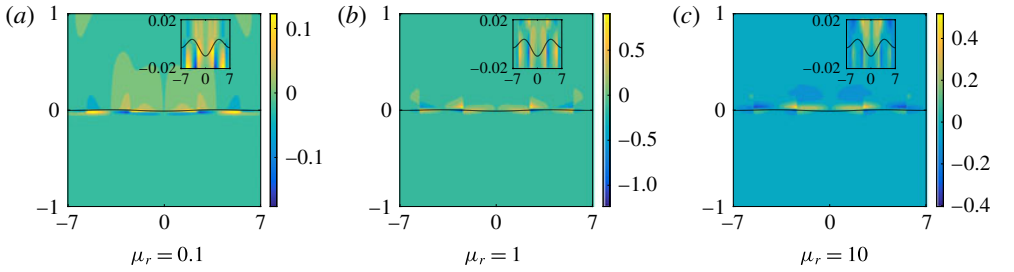


FIGURE 7. (Colour online) See inset: top–bottom vorticity asymmetry $\Omega^{\mathcal{U}}(0, t)/\Omega^{\mathcal{L}}(0, t)$ at the linearised interface $z = 0$ changes by varying the viscosity ratio from $\mu_r < 1$ through $\mu_r = 1$ to $\mu_r > 1$. Cases (*a*) 10, (*b*) 11 and (*c*) 12.

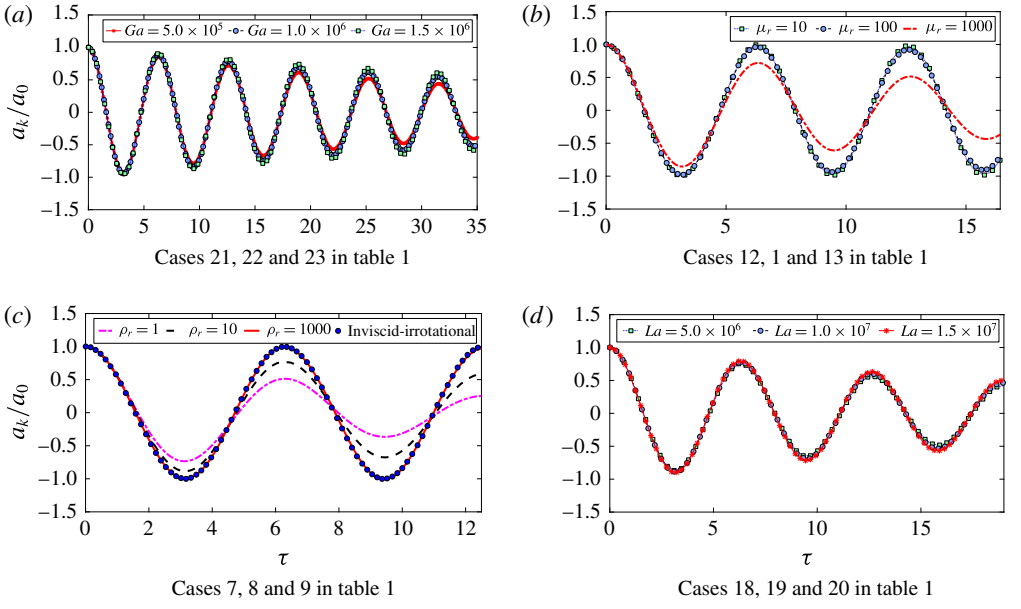


FIGURE 8. (Colour online) Amplitude versus τ with respect to all non-dimensional parameters.

$$H[\eta(r, t)] = \int_0^L r\eta(r, t)\mathrm{J}_0(kr)\,\mathrm{d}r, \tag{5.2}$$

where L is the radial domain length used in the simulations. Hankel transform $H[\eta]$ is done for the interface $\eta(r, t)$ using an in house subroutine written in MATLAB (2015). The code was validated by reproducing the results given in Mathematica (2017) for $L = 1000$ ($L \to \infty$ recovers the Hankel transform). The numerical noise in the evaluation of (5.2) reduces as $L \to \infty$. As the domain size $[0, 7.0155] \times [0, 7.0155]$ produced a very noisy transform, we performed additional larger domain simulations ($[0, 35.3323] \times [0, 35.3323]$, cases 24, 25 and 26 in table 1) for evaluating the Hankel transform. In all cases, we checked and found that the interface evolution was independent of the domain size to working precision. The interface evolution is shown in figure 9 while the corresponding Hankel transform of the interface is

https://doi.org/10.1017/jfm.2017.443 Published online by Cambridge University Press

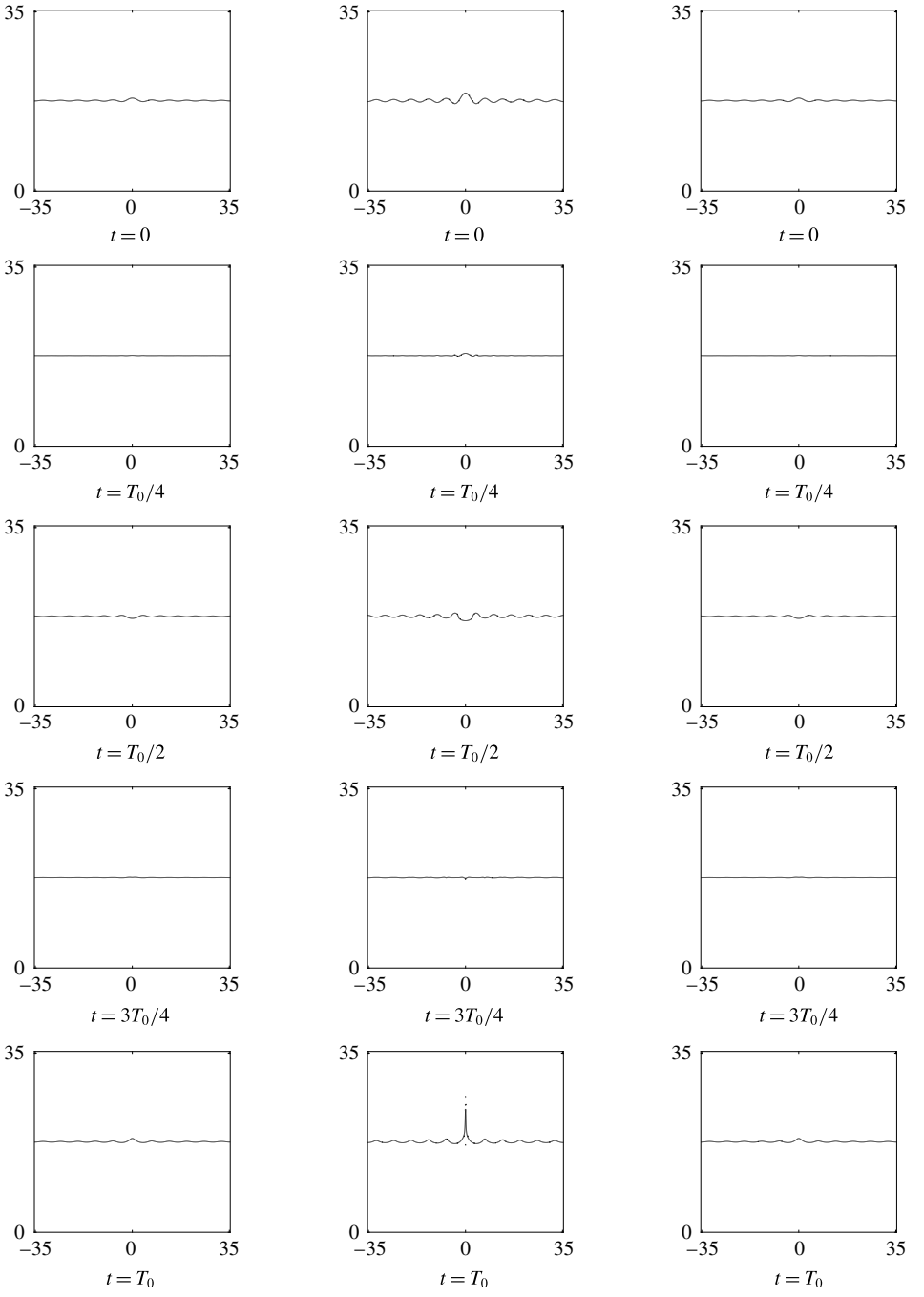


FIGURE 9. Interface for $\epsilon = 0.5$, 1.5 and 3.5 for cases 24, 25 and 26 in table 1.

shown in figure 10. The columns in both figures represent $\epsilon = 0.5$, 1.5 and 3.5 from left to right with each figure showing the interface (figure 9) and Hankel transform (figure 10) at various instants of time. It is seen that the second mode $k = 2$ starts

https://doi.org/10.1017/jfm.2017.443 Published online by Cambridge University Press

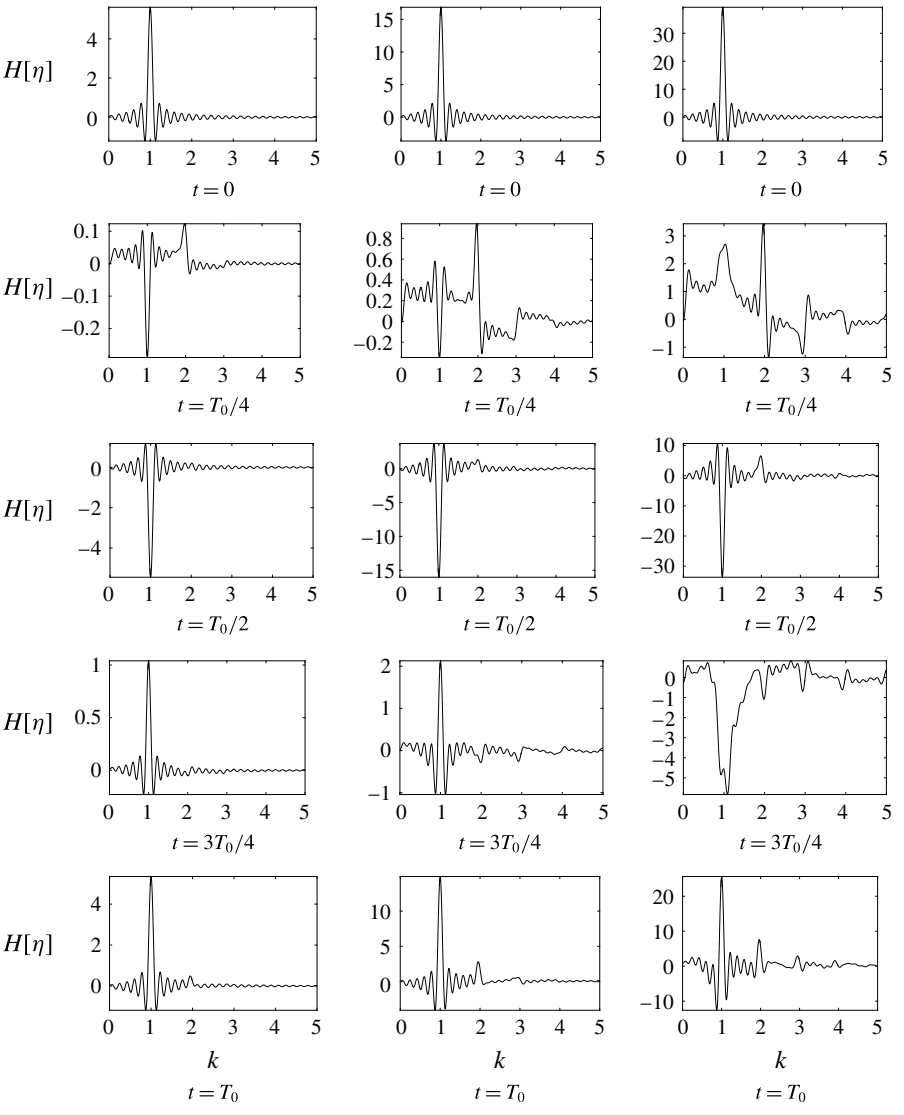


FIGURE 10. Hankel transform for cases 24, 25 and 26 in table 1 corresponding to the interface profiles in figure 9. Note that the vertical scale of the figures are not the same.

appearing with a magnitude comparable to $k = 1$ for $\epsilon = 1.5$. For $\epsilon = 3.5$, the second, third and fourth modes ($k = 2$, 3 and 4) also appear. It is interesting to note that for ϵ greater than 0.5, at the end of one inviscid time period, higher modes survive along with the initial mode $k = 1$. Note that in figure 9 last column, the interface becomes a multivalued function of radius near $r = 0$. The Hankel transform for this case was obtained by excluding this small region of multivaluedness near $r = 0$. Figure 11, represents an instantaneous snapshot of the interface. A qualitative aspect of nonlinearity is clearly visible from the picture which shows that the crests are sharp while the troughs are rounded. This is reminiscent of cnoidal solutions of the Korteweg-de Vries equation (Dasgupta, Tomar & Govindarajan 2015). In figure 12(a), we plot the maximum height H_m reached by the jet as a function of initial amplitude,

https://doi.org/10.1017/jfm.2017.443 Published online by Cambridge University Press

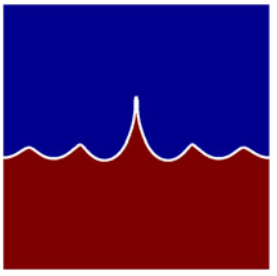


FIGURE 11. (Colour online) Sharp crests and rounded troughs – case 28 in table 1.

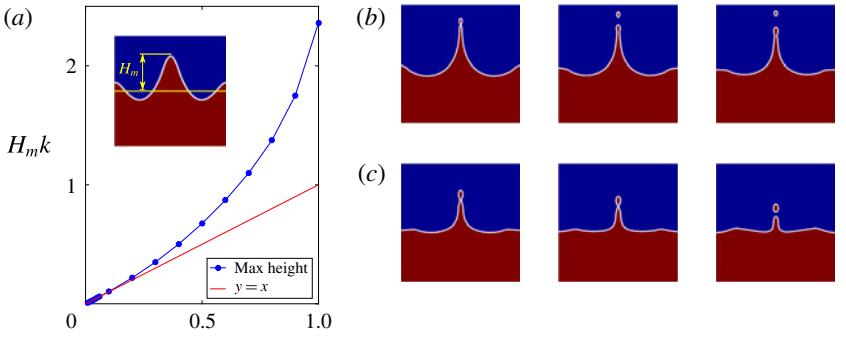


FIGURE 12. (Colour online) (*a*) Maximum jet height versus perturbation amplitude – variation of $H_m k$ with ϵ. All other parameters are for case 1 in table 1. The inset shows how H_m is measured. The $y = x$ line is for visual reference to show the onset of jetting. (*b*) Droplet pinch off for an advancing jet – case 27 in table 1. (*c*) Pinch off in a receding jet – case 28 in table 1.

when no droplet pinch off is yet observed. The inset of figure 12(*a*) shows the way we measure H_m in our simulations i.e. when the jet has reached its maximum vertical extent. Figure 12(*b*) shows droplet pinch off for an advancing jet while figure 12(*c*) shows the same for a receding jet. The two simulations differ in their values of viscosity ratio μ_r only.

6. Conclusions and future work

In this study, we have solved the linearised IVP of an axisymmetric perturbation initialised as a Bessel mode on the interface of two radially unbounded, viscous immiscible fluids. We find that a small-amplitude Bessel mode evolves temporally in the same way as a spatial Fourier mode in planar geometry. We compare our analytical results to the normal mode approximation and to DNS. For small amplitudes, the DNS results compare extremely well to the solution of the IVP. The normal mode approximation is found to be good at very early and late times with deviations at intermediate times. The vorticity jump across the interface is found to depend in general both on the density and viscosity ratios of the two fluids. We show that by choosing the viscosity ratio to be unity, the magnitude of this jump can be reduced. Upon increasing the initial amplitude of perturbation, nonlinear effects produce qualitatively new features not present in the linearised IVP solution. Notable among these is the formation of a jet at the axis of symmetry which can rise to a height

https://doi.org/10.1017/jfm.2017.443 Published online by Cambridge University Press

much greater than the parent perturbation. Depending on the viscosity ratio, the jet may undergo end pinch off while advancing or receding, leading to daughter droplet formation. A relation between the maximum jet height and the initial perturbation amplitude is obtained. Parametric studies are reported for the effect of change of parameters on under-damped oscillations. The emergence of new modes is studied using the Hankel transform of the interface.

The results obtained in this study will be useful in varied contexts. The analytical formulae presented here for $a_k(t), p_v(r, z, t)$ and $\omega_\theta(r, z, t)$ are useful for benchmarking codes. From a more fundamental perspective, our analytical results for a single Bessel mode can be used to solve the axisymmetric Cauchy–Poisson problem (for arbitrary initial conditions) in closed form, taking into account viscosity and inertia in both the fluids. For general initial conditions which excite a large (an uncountable infinite) number of modes at $t = 0$, one would expect deviations from predictions made by the normal mode approximation when compared to IVP predictions. A comparison of the contribution of the continuous spectrum modes *vis-a-vis* discrete normal modes for general initial conditions, requires more simulations and analysis. This is currently underway and will be presented in a forthcoming publication. The study of jetting and subsequent droplet pinch off and the role of interfacial vorticity in these, will help obtain better and more detailed understanding of droplet impact on a deep pool. Finally, the linearised, unsteady, base state solution presented here will find applications in the study of forced oscillations like Faraday waves.

Acknowledgements

R.D. and P.K.F. acknowledge Industrial Research and Consultancy Centre (IRCC), IIT Bombay for a start up grant and for supporting the latter's PhD fellowship. We thank Science and Engineering Research Board (SERB), Dept. of Science and Technology, Govt. of India (grant no. EMR/2016/000830) for financial support for a related study of interfacial oscillations. R.D. acknowledges a useful discussion with R. Govindarajan on vorticity asymmetry across an interface.

Supplementary data

Supplementary data is available at https://doi.org/10.1017/jfm.2017.443.

REFERENCES

ABATE, J. & WHITT, W. 2006 A unified framework for numerically inverting laplace transforms. *INFORMS J. Comput.* **18** (4), 408–421.

ABRAMOWITZ, M. & SEGUN, I.-A. 1970 *Handbook of Mathematical Functions with Formulas, Graphs, and Mathematical Table*. Dover.

BALMFORTH, N. J. & MORRISON, P. J. 1995 Singular eigenfunctions for shearing fluids i. https://web2.ph.utexas.edu/m̃orrison/95IFSR692_morrison.pdf.

BARTOLO, D., JOSSERAND, C. & BONN, D. 2006 Singular jets and bubbles in drop impact. *Phys. Rev. Lett.* **96** (12), 124501.

BECHHOEFER, J., EGO, V., MANNEVILLE, S. & JOHNSON, B. 1995 An experimental study of the onset of parametrically pumped surface waves in viscous fluids. *J. Fluid Mech.* **288**, 325–350.

BECKER, E., HILLER, W. J. & KOWALEWSKI, T. A. 1991 Experimental and theoretical investigation of large-amplitude oscillations of liquid droplets. *J. Fluid Mech.* **231**, 189–210.

BEETHAM, E., KENCH, P. S., O'CALLAGHAN, J. & POPINET, S. 2016 Wave transformation and shoreline water level on funafuti atoll, tuvalu. *J. Geophys. Res.* **121** (1), 311–326.

https://doi.org/10.1017/jfm.2017.443 Published online by Cambridge University Press

BELL, J. B, COLELLA, P. & GLAZ, H. M. 1989 A second-order projection method for the incompressible Navier–Stokes equations. *J. Comput. Phys.* **85** (2), 257–283.

BRACKBILL, J. U., KOTHE, D. B. & ZEMACH, C. 1992 A continuum method for modeling surface tension. *J. Comput. Phys.* **100** (2), 335–354.

BRØNS, M., THOMPSON, M. C., LEWEKE, T. & HOURIGAN, K. 2014 Vorticity generation and conservation for two-dimensional interfaces and boundaries. *J. Fluid Mech.* **758**, 63–93.

BUSH, J. 2013 Lecture notes – 18.357 interfacial phenomena, 5.4 appendix b, pp. 21. https://ocw.mit.edu/courses/mathematics/18-357-interfacial-phenomena-fall-2010/lecture-notes/MIT18_357F10_lec_all.pdf.

CHANDRASEKHAR, S. 1961 *Hydrodynamic and Hydromagnetic Stability*. Courier Dover Publications.

DASGUPTA, R., TOMAR, G. & GOVINDARAJAN, R. 2015 Numerical study of laminar, standing hydraulic jumps in a planar geometry. *Eur. Phys. J.* E **38** (5), 1–14.

DEBNATH, L. 1994 *Nonlinear Water Waves*. Academic.

DENNER, F. 2016 Frequency dispersion of small-amplitude capillary waves in viscous fluids. *Phys. Rev.* E **94** (2), 023110.

DENNER, F., PARÉ, G. & ZALESKI, S. 2017*a* Dispersion and viscous attenuation of capillary waves with finite amplitude. *Eur. Phys. J.* **226**, 1229–1238.

DENNER, F., PARÉ, G. & ZALESKI, S. 2017*b* Dispersion and viscous attenuation of capillary waves with finite amplitude (supporting data). https://zenodo.org/record/259434#.WRmAkhJ97vt.

DIXIT, H. N. & GOVINDARAJAN, R. 2010 Vortex-induced instabilities and accelerated collapse due to inertial effects of density stratification. *J. Fluid Mech.* **646**, 415–439.

DRAZIN, P. G. & REID, W. H. 2004 *Hydrodynamic Stability*. Cambridge University Press.

FARADAY, M. 1831 On a peculiar class of acoustical figures; and on certain forms assumed by groups of particles upon vibrating elastic surfaces. *Phil. Trans. R. Soc. Lond.* **121**, 299–340.

FARSOIYA, P. K., MAYYA, Y. S. & DASGUPTA, R. 2017 Supplementary material. doi:10.1017/jfm.2017.443.

GEKLE, S. & GORDILLO, J. M. 2010 Generation and breakup of worthington jets after cavity collapse. Part 1. Jet formation. *J. Fluid Mech.* **663**, 293–330.

GOODRIDGE, C. L., SHI, W. T., HENTSCHEL, H. G. E. & LATHROP, D. P. 1997 Viscous effects in droplet-ejecting capillary waves. *Phys. Rev.* E **56** (1), 472–475.

HARRISON, W. J. 1908 The influence of viscosity on the oscillations of superposed fluids. *Proc. Lond. Math. Soc.* **2** (1), 396–405.

HENDERSON, D. M. & MILES, J. W. 1994 Surface-wave damping in a circular cylinder with a fixed line. *J. Fluid Mech.* **275**, 285–299.

HIRT, C. W. & NICHOLS, B. D. 1981 Volume of fluid (vof) method for the dynamics of free boundaries. *J. Comput. Phys.* **39** (1), 201–225.

JAMES, A. J., VUKASINOVIC, B., SMITH, M. K. & GLEZER, A. 2003 Vibration-induced drop atomization and bursting. *J. Fluid Mech.* **476**, 1–28.

JOSEPH, D. D. 2003 Viscous potential flow. *J. Fluid Mech.* **479**, 191–197.

KUNDU, P. K. & COHEN, I. M. 2002 *Fluid Mechanics*, 2nd edn. chap. Appendix B, pp. 710–714. Academic.

LAMB, H. 1932 *Hydrodynamics*. Cambridge University Press.

LEAL, L. G. 2007 *Advanced Transport Phenomena: Fluid Mechanics and Convective Transport Processes*. Cambridge University Press.

LI, Y. & UMEMURA, A. 2014 Threshold condition for spray formation by faraday instability. *J. Fluid Mech.* **759**, 73–103.

LONGUET-HIGGINS, M. S. 2001 Vertical jets from standing waves. In *Proceedings of the Royal Society of London A: Mathematical, Physical and Engineering Sciences*, vol. 457, pp. 495–510. The Royal Society.

MACK, L. R. 1962 Periodic, finite-amplitude, axisymmetric gravity waves. *J. Geophys. Res.* **67** (2), 829–843.

MATHEMATICA 2017 Perform numerical hankel transform. https://www.wolfram.com/mathematica/new-in-8/new-and-improved-core-algorithms/perform-numerical-hankel-transform.html.

MATLAB 2015 *MATLAB and Statistics Toolbox Release 2015b*. The MathWorks Inc.

https://doi.org/10.1017/jfm.2017.443 Published online by Cambridge University Press

McClure, T. 2016 Numerical inverse laplace transform. https://in.mathworks.com/matlabcentral/fileexchange/39035-numerical-inverse-laplace-transform.

Menikoff, R., Mjolsness, R. C., Sharp, D. H., Zemach, C. & Doyle, B. J. 1978 Initial value problem for Rayleigh–Taylor instability of viscous fluids. *Phys. Fluids* **21** (10), 1674–1687.

Miles, J. & Henderson, D. 1990 Parametrically forced surface waves. *Annu. Rev. Fluid Mech.* **22** (1), 143–165.

Miles, J. W. 1968 The cauchy-poisson problem for a viscous liquid. *J. Fluid Mech.* **34** (2), 359–370.

Perinet, N., Juric, D. & Tuckerman, L. S. 2009 Numerical simulation of faraday waves. *J. Fluid Mech.* **635**, 1–26.

Popinet, S. 2003 Gerris: a tree-based adaptive solver for the incompressible euler equations in complex geometries. *J. Comput. Phys.* **190** (2), 572–600.

Popinet, S. 2013, Air-water capillary wave. http://gfs.sourceforge.net/tests/tests/capwave.html#toc15.

Popinet, S. 2014 Basilisk. http://basilisk.fr.

Popinet, S. 2015 A quadtree-adaptive multigrid solver for the serre–green–naghdi equations. *J. Comput. Phys.* **302**, 336–358.

Prosperetti, A. 1976 Viscous effects on small-amplitude surface waves. *Phys. Fluids* **19** (2), 195–203.

Prosperetti, A. 1980 Normal-mode analysis for the oscillations of a viscous-liquid drop in an immiscible liquid. *J. de Méc.* **19** (1), 149–182.

Prosperetti, A. 1981 Motion of two superposed viscous fluids. *Phys. Fluids* **24** (7), 1217–1223.

Puthenveettil, B. A. & Hopfinger, E. J. 2009 Evolution and breaking of parametrically forced capillary waves in a circular cylinder. *J. Fluid Mech.* **633**, 355–379.

Rajchenbach, J. & Clamond, D. 2015 Faraday waves: their dispersion relation, nature of bifurcation and wavenumber selection revisited. *J. Fluid Mech.* **777**, R2.

Stokes, G. G. 1851 On the effect of the internal friction of fluids on the motion of pendulums. *Trans. Camb. Phil. Soc.* **9**, 8.

Sweeney, H., Kerswell, R. R. & Mullin, T. 2013 Rayleigh-Taylor instability in a finite cylinder: linear stability analysis and long-time fingering solutions. *J. Fluid Mech.* **734**, 338.

Taylor, G. 1953 An experimental study of standing waves. In *Proceedings of the Royal Society of London A: Mathematical, Physical and Engineering Sciences*, vol. 218, pp. 44–59. The Royal Society.

Thorpe, S. A. 1968 On standing internal gravity waves of finite amplitude. *J. Fluid Mech.* **32** (03), 489–528.

Trinh, E. & Wang, T. G. 1982 Large-amplitude free and driven drop-shape oscillations: experimental observations. *J. Fluid Mech.* **122**, 315–338.

Tripathi, M. K., Sahu, K. C. & Govindarajan, R. 2014 Why a falling drop does not in general behave like a rising bubble? *Sci. Rep.* **4**, 4771.

Tsai, C. S., Mao, R. W., Lin, S. K., Zhu, Y. & Tsai, S. C. 2014 Faraday instability-based micro droplet ejection for inhalation drug delivery. *Technology* **2** (01), 75–81.

Wolfram Research Inc. 2010 *Mathematica 10.0*.

Zeff, B. W., Kleber, B., Fineberg, J. & Lathrop, D. P. 2000 Singularity dynamics in curvature collapse and jet eruption on a fluid surface. *Nature* **403** (6768), 401–404.

https://doi.org/10.1017/jfm.2017.443 Published online by Cambridge University Press